Calculation of Positive-Sequence and Zero-Sequence Impedances of Three-Phase Submarine Cables

K. F. Goddard, *Member, IEEE,* J. Rzempołuch, *Member, IEEE,* S. Chaudhary, *Member, IEEE,* G. Callender, *Member, IEEE*, P. Lewin, *Fellow, IEEE*

***Abstract*—This paper describes semi-analytical calculation methods for the positive-sequence and zero-sequence impedances of 3-phase armored cables with solid sheaths and a single armor layer. Separate equivalent circuits are defined for these two impedances. Subsequently, circuit component values are calculated based on 2D field equations, with some 3D effects modeled. The existing approach for calculating zero-sequence impedance is corrected and expanded by inclusion of additional inductances due to solenoidal fields and magnetic armor effects. 3D finite-element models of cables with magnetic and non-magnetic armor are used to assess the accuracy of our circuit models; discrepancies are less than 3% at frequencies between 50 Hz and 5 kHz. Python code with the implementation of the method is provided for accessibility.**

***Index Terms*—Sequence Impedance Calculation, Armored Cables.**

I. Introduction

THE large-scale deployment of offshore wind turbines has greatly increased the use of three-phase submarine cables. Consequently, it has become more important to understand the impedance characteristics of such cables. For integration with the grid, transient stability studies are often required. For these, the frequency-dependence of the cable impedances is also important; frequencies up to a few kHz may need to be considered [1]. Such data may also be required for tuning any inverters that are connected to the cable.

Calculation of impedances is possible using Finite Element Analysis (FEA) models. Tools for 2D FEA are the most widely available, and these models have lower computational costs. However, modelling the cable in 2D can lead to large errors; as the twist of the cores and armour are not included in the model it can predict fictitious circulating currents. This problem can be overcome by connecting an external circuit to the model to ensure that the currents in the armour wires are equal by connecting them in series [2]; this is known as a 2.5D model. These models still have some limitations that may be significant; in particular, various solenoidal effects are not represented.

To model solenoidal effects without losing the direct connection between the geometry of the model and that of the cable, 3D models are required. In the past, 3D FEA models were prohibitively computationally expensive as they required large lengths of the cable to be modelled. However, with the introduction of twisted-periodic symmetry boundaries into FEA tools, it became possible to develop short twisted 3D models, which have greatly reduced computational cost [3], [4]. In this paper, the presented analytical methods are validated using modified versions of the model in [3]. Although 3D FEA models are accurate, the geometry of such models can be complex which makes construction and meshing of the model difficult; thus, significant human effort may be required to adapt the model for a different cable design or a different frequency range.

As capable FEA software is expensive and may be unavailable, some low-cost alternatives have been developed. The simplest of these is Multi-Conductor Analysis (MCA) which works by dividing each conductor into sub-conductors that are small enough to justify assuming uniform current density in each one. Assuming circular sub-conductors, each one is defined by its position, effective radius and resistance per unit length. From this data, a mutual-impedance matrix is produced, which can be used to estimate the current and loss in each sub-conductor arising from any set of applied voltages. The method neglects the effects of magnetization and depends on human judgement to choose appropriate positions radii and resistances for the sub-conductors; it is a 2D method, but it can be extended to produce a 2.5D model using multi-dimensional matrices. MCA can give useful estimates of sequence impedances [5], [6], [7] but its reliance on human judgement makes validation difficult.

Method of Moments with a Surface Operator (MOM-SO) presented in [8] is a more computationally efficient approach compared to MCA and finite element methods. In this method, conductors are represented by equivalent current sheets, which are defined as Fourier series; this makes the method easy to automate. The Fourier coefficients are determined using a surface admittance operator, while the relationship between the electric field and the surface currents determines the impedance of the system. This method captures skin and proximity effects and can be used for solid and hollow conductors. The method can model permeable materials and can be extended to 2.5D [9] to suppress fictitious circulating currents. In [4], a 2.5D MOM-SO model is compared to the corresponding 2.5D FEA model, and they are observed to be in excellent agreement.

Both MOM and MCA methods are limited to 2D or 2.5D representations that cannot model longitudinal magnetic flux in armour wires or axial flux driven by circumferential currents.

Kevin Goddard, Joanna Rzempołuch, Sunny Chaudhary, George Callender, and Paul Lewin are with the Tony Davies High Voltage Laboratory, University of Southampton, Southampton SO17 1BJ, United Kingdom (e-mail: kfg@ecs.soton.ac.uk; jr9g20@soton.ac.uk; sc.chaudhary@soton.ac.uk; gmc1f17@soton.ac.uk; pll@soton.ac.uk)

In [10], it is claimed that MOM-SO can be extended to include solenoidal effects, but the method is difficult to reproduce from the information given in the paper and is not validated against impedance values. The transient studies undertaken in [4] demonstrated large differences between a short-twisted 3D FEA model and 2.5D models of the same cable, suggesting that the factors omitted in 2.5D methods can be significant. However, 3D models have much higher computational cost and may require significant human effort and expertise. We aim to overcome some of the limitations of 2.5D models without the high cost of using 3D FEA models.

Alternatively, methods developed for calculation of armor losses can be used to estimate positive-sequence impedances. The two main existing approaches are CIGRE Technical Brochure 908 [11], and Goddard et al. [12]. In this work, minor alterations to the method in [12], relating to 3D effects, are made to further improve the method's accuracy.

While there are many papers on methods of calculating positive-sequence impedance, methods for calculating zero-sequence impedances that include the effects of magnetic armour and solenoidal effects are more rare. Section 4.2 of CIGRE TB 531 presents various impedance expressions including a zero-sequence impedance calculation, but these do not consider the frequency dependence of the internal inductance of the conductors or proximity effects; hence, they have limited applicability for armored 3-phase cables. The most commonly used method applicable to submarine cables has been presented in Kvartz et al. [13], where corrections to the methods from CIGRE 531 were introduced to include the armor return path, and include the skin and proximity effect and lay factors using loss expressions from IEC 60287 [14]. This reliance on the standards, [14], can lead to inaccuracies as it does not accurately capture the influence of magnetic armor [12]. The method developed in [13] contains some errors, neglects the influence of the solenoidal inductances and fails to account for the magnetic armour accurately. Furthermore, it is only validated for 50 Hz and a cable with non-magnetic armor. In this paper, the method in [13] is modified to include the solenoid effects and the effects of magnetic armour, and to correct some errors. This is the main contribution of this paper, and results in a significantly better agreement with an FEA model. The results are analyzed for a range of frequencies 50 Hz – 5kHz and the method is validated for both magnetic and non-magnetic armor cases.

Additionally, we have extended the 3D FEA model based on [3] to make it suitable for verification of our zero-sequence calculations. This is required because the field of zero-sequence currents extends much further from the cable, while extending the short-twisted model into the sea would not be valid (as the sea does not spiral around the cable). The models used for validation in this paper were created by coupling a short-twisted 3D model with a 2D model of the exterior domain that extends out to a radius of 2 km. The coupling between the two components (2D and 3D) is performed within one model using COMSOL functions. The method of combining results from 2D and 3D models used in [4] is valid for their application, in which the fields driven by conductor, sheath and armour currents are modelled separately, to facilitate the calculation of the full series-impedance matrix. However, it would not be valid for this application where the zero-sequence impedance is calculated directly, while allowing the return current to divide freely between sheath, armour and ground return paths.

II. Modeling Approach

We use simplifying approximations to derive semi-analytical calculation methods that can be used without an FEA package or an experienced user. Our modeling approach is as follows:

1) Circuit models of the cable system are created; the model used for positive-sequence calculations is represented by a complex impedance matrix; the currents in conductors and sheaths are represented by Fourier series, while armour currents are neglected, as per [12]. The circuit used for the zero-sequence calculations includes the armour current but allows only scalar values of currents; it is represented by a circuit diagram, based on the approach of [13], with only 2-node impedance components.
2) The impedances in the circuit models are calculated using 2D field equations, assuming zero-thickness sheaths and armour. Length factors are used to allow for the increased lengths of conductors, screens and armour caused by their lay angles.
3) Solenoidal inductances and mutual inductances are calculated, and appropriate adjustments are made to the component impedances. In the zero-sequence model, the mutual inductance is accounted for by adjusting the values of adjacent circuit components.
4) Alteration to impedances due to magnetic armor is calculated. The armour is represented as a layer with anisotropic permeability modeled according to [12]. The positive- and zero-sequence models use different methods to capture the effect of the armor's permeability as there is a current flowing in the armor in the zero-sequence case which can be omitted in the positive-sequence case.
5) Calculate the overall impedances. For the positive-sequence model, this requires solution of the simultaneous equations; for the zero-sequence model impedances can be combined in series or parallel until a single impedance remains.

III. Zero-Sequence Model

In this section, the method for the calculation of zero-sequence impedance is presented. This method is based on the one described in [13]. Some expressions are corrected and a method to include solenoidal and magnetic armor effects, not included in [13], is developed.

For this method, the thickness of sheaths and armor are neglected, but their resistances are modeled. The circuit model is defined by a circuit diagram that has only 2-node impedance components; this avoids the need to solve simultaneous equations, but it imposes some limitations on the cable configurations that can be modeled. Fig. 1 shows a

circuit diagram adapted from [13]. The inductances in this method are calculated for 3 sets of current loops: Loop 1 currents flow in the conductors and return in their sheaths or screens; Loop 2 currents flow in the sheaths and return in the armor; and Loop 3 currents flow in the armor and return in the ground; the factors of 3 in the Loop 3 impedances arise because the currents for all three phases share a single path.

Even though the equations are derived using 2D field equations, the lay angle of conductors, screens and armor are included as length factors in equations (LF_C, LF_A) to account for the increased impedance due to the longer path in 3D.

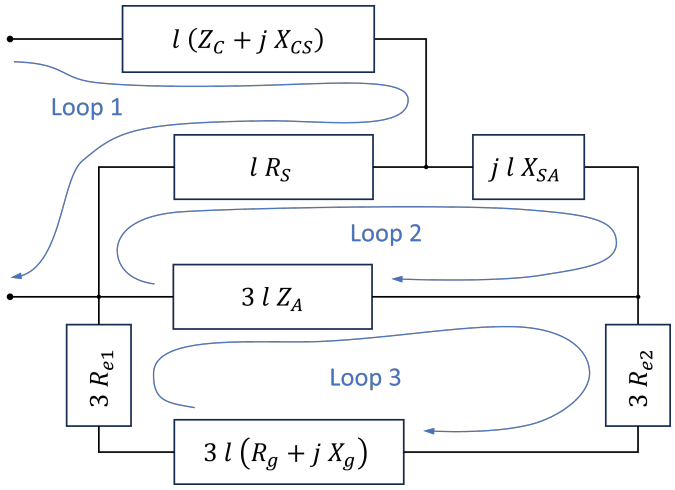

Fig. 1. Revised circuit diagram for zero-sequence impedance, adapted from [13].

In Fig. 1, Z_C is the internal impedance of a conductor, X_{CS} is the reactance due to leakage flux between a conductor and its sheath, R_S is the resistance of a sheath, Z_A is the internal impedance of the armor, and X_{SA} is the reactance to a Loop-2 current, including the contribution of mutual inductances between these currents, but excluding any contribution from Z_A. $R_g + jX_g$ is the internal impedance of the ground-return path, excluding end effects. All these impedances are per unit cable length.

Initially, we calculate the inductances for 2D geometry with zero-thickness sheaths and armor. Inductances due to solenoid effects and effects of magnetic armor are added later.

$$Z_C = R_C \frac{1}{2} \alpha r_C I_0(\alpha r_C)/I_1(\alpha r_C) \tag{1}$$

where R_C is the DC resistance of the conductor per unit cable length, r_C is the conductor radius, I_0 and I_1 are modified Bessel functions of the first kind, and

$$\alpha^2 = j\omega\sigma\mu_0 \tag{2}$$

where j is the imaginary number, ω is the angular frequency, σ is the average electrical conductivity of the conductor, and μ_0 is the magnetic permeability. Equation (1) differs from the one used in [13], but the differences are not significant. We use analytical Bessel-function expressions [15], while [13] uses simplified expressions with resistance from IEC 60287.

$$X_{CS} = LF_C \frac{\omega\mu_0}{2\pi} \ln(r_S/r_C), \tag{3}$$

where LF_C is the ratio of the conductor length to the cable length, and r_S is the radius of the sheaths. We have removed the armor-enhancement factor used in [13], as the magnetic fields of the Loop-1 currents are largely confined inside the sheaths, while the armor is outside.

$$X_{SA} = LF_C \frac{\omega\mu_0}{2\pi} \ln(r_A^3/s^2 r_S), \tag{4}$$

where r_A is the mean radius of the armor, and s is the spacing of the conductors. Here too, we have removed the armor-enhancement factor used in [13], as the method of allowing for the presence of magnetic armor has been replaced by the one described in Section III B. For non-magnetic armor, we assume $Z_A = R_A$; as in [13], we neglect any change in inductance caused by assuming that the armour current is uniformly distributed on a surface at r_A. For consistency, we therefore subtract the low-frequency internal reactance of non-magnetic armour from the internal impedance of magnetic armor,

$$Z_A = R_A \frac{1}{2} \alpha r_f I_0(\alpha r_f)/I_1(\alpha r_f) - j\omega LF_A \mu_0/(8\pi n_f), \tag{5}$$

where R_A is the DC resistance of the armor per unit cable length, r_f is the radius of an armor wire, LF_A is the length of an armor wire per unit cable length, and n_f is the number of armor wires; here,

$$\alpha^2 = j\omega\sigma\mu_0\mu_r, \tag{6}$$

where σ is the electrical conductivity of the armor wire, and μ_r is its relative permeability. Our expressions for the ground-return impedance, $R_g + jX_g$, are based on those given in [13], but we do not apply the factor LF_A to X_g, as this is not an appropriate method of allowing for the effect of the armor lay-angle on this impedance; these solenoid effects are considered in Section III A.

$$R_g = \omega\mu_0/8, \tag{7}$$

$$X_g = \omega \frac{\mu_0}{2\pi} \ln(D_e/r_A), \tag{8}$$

where D_e is the effective distance to the return current,

$$D_e = 400/\sqrt{\sigma f} \tag{9}$$

σ is the electrical conductivity of the surrounding material, and f is the frequency [13]; the constant 400 is appropriate when the variables have SI units.

In our implementation, we neglect the earth resistances R_{e1} and R_{e2}, and calculate the impedance per unit length; hence the factors of the cable length l are also removed; we do this to reduce the number of input parameters required. Note that for land applications, a different expression for the ground return radius would be needed to account for the absence of any return current above the ground surface.

A. Including Solenoidal Inductances

The circuit from Fig. 1 was modified to introduce inductances from solenoid effects, as shown in Fig. 2. Usually, including a mutual-inductance component in the circuit would require the solution of simultaneous equations to calculate the

overall impedance. However, in the simple case with single-layer armor and solid sheaths, this is not required; we can eliminate the mutual inductance component by changing the impedances of the adjacent circuit components (Z_A,X_{SA},X_g).

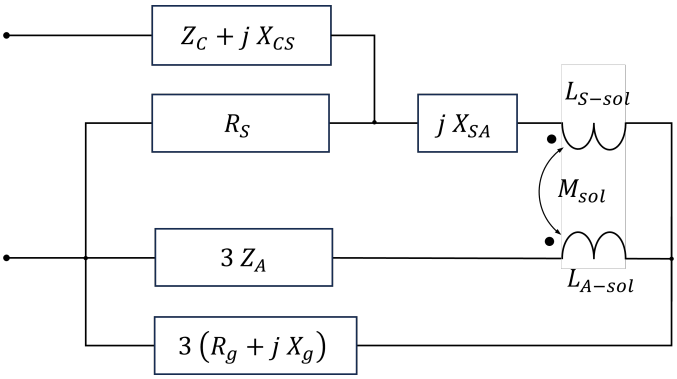

Fig. 2. Circuit diagram with solenoidal inductances.

All three solenoidal inductances in the circuit diagram are calculated using the same principle. Axial flux within the cylinder of radius r_A is driven by the armor current. Within the cylinder of radius c, power-core currents also drive axial flux. Thus, these inductances are:

$$L_{S-sol} = 3\mu_0\pi c^2/LL_C^2 \tag{10}$$

$$M_{sol} = \pm 3\mu_0\pi c^2/(LL_C LL_A) \tag{11}$$

$$L_{A-sol} = 3\mu_0\pi r_A^2/LL_A^2 \tag{12}$$

c is the pitch-circle radius of the conductors, LL_C is the lay length of the conductors, and LL_A is the lay length of the armor wires. M_{sol} is positive for unilay armor and negative for contralay armor.

The resulting inductances to the loop currents are:

$$\Delta L_{Loop2} = L_{S-sol} + L_{A-sol} - 2M_{sol}; \tag{13}$$

$$\Delta L_{Loop3} = L_{A-sol}; \tag{14}$$

$$\Delta M_{2,3} = M_{sol} - L_{A-sol}; \tag{15}$$

From these expressions, we can calculate the required changes to the values of adjacent impedance components.

$$\Delta 3Z_A = -j\omega\Delta M_{2,3} = j\omega(L_{A-sol} - M_{sol}); \tag{16}$$

$$\Delta X_{SA} = \omega(\Delta L_{Loop2} + \Delta M_{2,3}) = \omega(L_{S-sol} - M_{sol}); \tag{17}$$

$$\Delta X_g = \omega(\Delta L_{Loop3} + \Delta M_{2,3}) = \omega M_{sol}. \tag{18}$$

B. Allowing for Effects of Armor Permeability

In the positive-sequence case, because the lay length or direction of the armor differs significantly from that of the conductors, large circulating currents are not induced in the armor. However, in the zero-sequence case, analyzed in this section, the armor current should not be neglected. Additional 3D effects therefore arise from the lay angle of the armor wires. Axial flux driven by the armor current can induce voltages in the conductors and sheaths or screens. In this method, we use a hierarchical modeling approach for the armor; we use auxiliary 2D models to estimate the anisotropic characteristics of the armor layer, then use these to estimate its effect on the circuit characteristics. The auxiliary models estimate the reflected fields from an infinite flat layer of cylindrical wires in response to uniform applied fields, as per [12]; this requires many reflections to be calculated.

We first consider the additional self and mutual inductances to sheath and armor currents; then we calculate the changes in the component impedances required to represent these additional inductances. The equivalent circuit in Fig. 2. was modified to include the effects due to the armor's permeability, see Fig. 3. L_{S-perm} represents the additional self-inductance to the sheath current, L_{A-perm} is the additional inductance to the armor current and M_{perm} is the additional mutual inductance between the two currents.

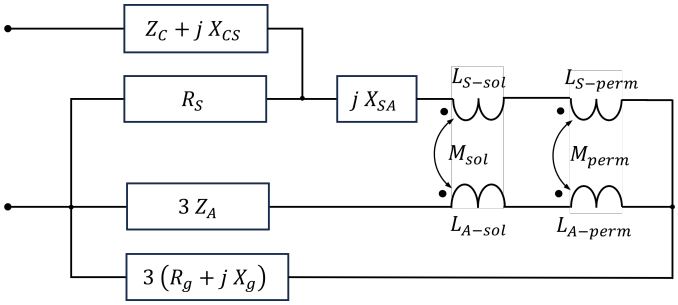

Fig. 3. Circuit diagram with solenoidal inductances and the inductances to the sheath and armor currents and armor permeability.

Initially, we consider the effect on the inductance to the enclosed sheath currents when these currents return in the ground. The additional inductance to the enclosed current, expressed in terms of magnetic energy, is given by,

$$3I^2\Delta L = \iiint H \cdot \Delta B dv. \tag{19}$$

We assume that the H-field imposed by zero-sequence currents is uniformly distributed around the circumference of the armor layer; this implies that the tangential component H_θ is dominant. With these assumptions, (19) gives the additional inductance per unit cable length

$$3\Delta L = \mu_0 2\pi r_A t_A \left(\left(\frac{H_l}{I}\right)^2 (\mu_l - 1) + \left(\frac{H_t}{I}\right)^2 (\mu_t - 1) \right), \tag{20}$$

where t_A is the effective thickness of the armor layer, H_l and H_t are the longitudinal and transverse components of the field imposed on the armor wires, while μ_l and μ_t are the effective relative permeabilities of the armor layer to these fields. The methods used to calculate t_A, μ_l, and μ_t are taken from [12].

As all 3 currents make equal contributions to the H-field,

$$H_\theta = \frac{3I}{2\pi r_A}, \tag{21}$$

where I is the total current of each power core. We also note that $H_l = H_\theta \sin\beta$ and $H_t = H_\theta \cos\beta$ where β is the lay angle of the armor. Substituting these expressions into

(20), we find that the permeability of the armour increases the inductance to the enclosed sheath and conductor currents by

$$L_{S-perm} = \frac{3\mu_0 t_A}{2\pi r_A}(\sin^2(\beta)(\mu_l - 1) + \cos^2(\beta)(\mu_t - 1)). \quad (22)$$

To test the validity of the uniform-field assumption, we consider the tangential field component of the magnetic field at radius r_A, driven by three straight line currents at radius c. In this simple 2D model, the tangential field differs from its average value by a factor of between $1/(1 + (c/r_A)^3)$ and $1/(1 - (c/r_A)^3)$. For the cable considered, the maximum deviation of H_θ is from the average is 16%, but the average value of H_θ^2 is increased by less than 1.1%. As magnetic armor will make the field more uniform, the assumption is clearly justified.

Next, we consider the inductance to armor current that returns in the ground and the mutual inductance between this current and the enclosed sheath current considered above. Whereas the H-field of the enclosed current varies little through the thickness of the armor, the field of the armor current varies greatly; see Fig. 4. We assume that the armor current can be represented as an equivalent current sheet with separate axial and circumferential components of the current density dependent on the armor's lay length. Following Ampère's law, the axial component of the current produces a purely circumferential H-field outside of the armor, H_{Ext}, whilst the circumferential component of the current produces a purely axial H-field inside, H_{Int}. Notice that only the transverse H-field component, H_t, varies between the inside and the outside of the armor layer. Therefore, the longitudinal flux contributes equally to both self-inductances and to the mutual inductance.

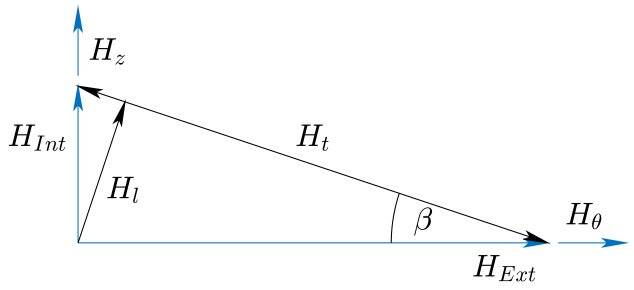

Fig. 4. H-fields in the armor driven by the armor current.

As the transverse flux in the armor is concentrated close to the mean armor radius where the gaps between the wires are small, we assume that the effective transverse field is the average of the internal and external field values.

$$\begin{aligned} H_t &= H_{Ext}(\cos(\beta) - \sin(\beta)\tan(\beta))/2 \\ &= H_{Ext}\left(\frac{\cos(\beta)}{2} - \frac{1-\cos^2(\beta)}{2\cos(\beta)}\right) \\ &= H_{Ext}\left(\cos(\beta) - \frac{1}{2\cos(\beta)}\right). \end{aligned} \quad (23)$$

Thus, following (20), the expression for the increase in the self-inductance to the armor current due to the magnetization is

$$\begin{aligned} L_{A-perm} =& \frac{3\mu_0 t_A}{2\pi r_A}\Bigg(\sin^2(\beta)(\mu_l - 1) \\ &+ \left(\cos(\beta) - \frac{1}{2\cos(\beta)}\right)^2(\mu_t - 1)\Bigg). \end{aligned} \quad (24)$$

Consequently, the mutual inductance is increased by

$$\begin{aligned} M_{perm} =& \frac{3\mu_0 t_A}{2\pi r_A}\Bigg(\sin^2(\beta)(\mu_l - 1) \\ &+ \cos(\beta)\left(\cos(\beta) - \frac{1}{2\cos(\beta)}\right)(\mu_t - 1)\Bigg). \end{aligned} \quad (25)$$

We can now determine the changes to the impedances of the circuit components required to represent magnetic armor using the calculations above, and analogues to (17), (16) and (18):

$$\Delta X_{SA} = \omega\frac{3\mu_0 t_A}{2\pi r_A}\cdot\frac{1}{2}(\mu_t - 1); \quad (26)$$

$$\Delta 3Z_A = j\omega\frac{3\mu_0 t_A}{2\pi r_A}\left(\frac{1}{4\cos^2(\beta)} - \frac{1}{2}\right)(\mu_t - 1); \quad (27)$$

$$\begin{aligned} \Delta 3X_g =& \omega\frac{3\mu_0 t_A}{2\pi r_A}(\sin^2(\beta)\cdot(\mu_l - 1) \\ &+ \left(\cos^2(\beta) - \frac{1}{2}\right)(\mu_t - 1)). \end{aligned} \quad (28)$$

Now that we have incorporated the inductances due to armor permeability and solenoidal fields into the simple impedance components, we can combine two impedances in parallel or in series until the circuit is reduced to a single impedance,

$$Z_0 = Z_C + jX_{CS} + \frac{R_S(\frac{3Z_A(R_g+jX_g)}{Z_A+(R_g+jX_g)} + jX_{SA})}{R_S + \frac{3Z_A(R_g+jX_g)}{Z_A+(R_g+jX_g)} + jX_{SA}}, \quad (29)$$

where appropriate components are adjusted by the changes in impedance calculated previously in this section.

IV. Positive-Sequence Model

This model is based on the one described in [12] with minor changes made regarding the conductor lay length. We now apply the conductor length factor LF_C to the interior 2D model to account for the increase in impedance. The use of the length factor is equivalent to increasing the permeability and resistivity of the interior domains by a factor of LF_C. Thus, the expression for the reflection factor f_r in [12] is replaced by

$$f_r = \frac{\mu_e - LF_C}{\mu_e + LF_C}. \quad (30)$$

where μ_e is the permeability of the armor and exterior in parallel. This alteration results in a reduction of the reflection factor as the relative permeability increases from 1 to LF_C.

Additionally, the conductor lay length causes the external field of the cable to be twisted; this increases the effective permeability of the exterior domain, as additional axial flux paths are available. We adjusted the effective permeabilities of the exterior to allow for the spiral geometry of the exterior

field. This adjustment slightly increases the reflection factors as it increases μ_e in (30). From electromagnetic theory, B_r, the radial component of B-field and H_θ, the circumferential component of the H-field, must be continuous across boundaries. The exterior permeability, μ_{ext}, is adjusted to fulfill this condition by ensuring that the ratio of B_r/H_θ is preserved in the 2D model such that

$$\mu_0\mu_{ext}\frac{H_{r_{2D}}}{H_{\theta_{2D}}} = \mu_0\mu_r\frac{H_{r_{3D}}}{H_{\theta_{3D}}} \tag{31}$$

where μ_r is equal to 1 as it is the permeability of the outside material and μ_{ext} is the adjusted permeability of the exterior that needs to be calculated. We can define the H-field as

$$\mathbf{H} = -\nabla\psi \tag{32}$$

where ψ is the magnetic scalar potential. Using separated solutions, as described in [16], we can define the magnetic scalar potential in 2D as

$$\psi_n = r^{-n}\cos(n\theta) \tag{33}$$

where n represents the spatial frequency of the circumferential variation. Using (32), we calculate the ratio in (31),

$$\frac{H_{r_{2D}}}{H_{\theta_{2D}}} = \frac{-\frac{\partial\psi}{\partial r}}{-\frac{1}{r}\frac{\partial\psi}{\partial\theta}} = \frac{-nr^{-n-1}\cos(n\theta)}{-nr^{-n-1}\cos(n\theta)} = 1. \tag{34}$$

Due to the twisted geometry in 3D, the magnetic scalar takes the form

$$\psi_n = K_n(n\Omega r)\cos(n(\theta - \Omega z)), \tag{35}$$

where K_n is a modified Bessel function of the second kind and Ω is equal to $2\pi/LL_C$, which captures the axial variation of the potential in 3D. The derivative of K_n is defined as

$$K_n'(x) = -\frac{1}{2}[K_{n-1}(x) + K_{n+1}(x)]. \tag{36}$$

Consequently, we can calculate the adjusted permeability of the exterior in the 2D solution using (31) and (34),

$$\begin{aligned}\mu_{ext} = \frac{H_{r_{3D}}}{H_{\theta_{3D}}} &= \frac{-n\Omega K_n'(n\Omega r)\cos(n(\theta-\Omega z))}{-\frac{n}{r}K_n(n\Omega r)\cos(n(\theta-\Omega z))} \\ &= \frac{n\Omega K_n'(n\Omega r)}{\frac{n}{r}K_n(n\Omega r)}.\end{aligned} \tag{37}$$

It should be noted that θ is chosen such that division by zero is avoided in (34) and (37).

The final formulation for the positive-sequence impedance is

$$Z_+ = Z_C + jX_{CS} + j\omega M_{1,:}Z^{-1}j\omega M_{:,1} + j\omega M_{1,1}, \tag{38}$$

where

$$Z = Z_{\text{int}} + j\omega M, \tag{39}$$

M is the mutual impedance matrix calculated as per [12], Z_{int} is the diagonal matrix with internal impedances of the specific unknown currents, Z_C is the internal impedance of the conductor, described by (1), and X_{CS} is the reactance due to leakage flux between a conductor and its sheath, described by (3).

V. Finite-Element Verification Models

To test the accuracy of our impedance calculations, we have built 3D finite-element models using COMSOL Multiphysics 6.3 software based on the model from [3]. The model represents a short length of cable, just sufficient for one armour wire to pass each conductor; its two ends are connected by a twisted periodic boundary condition, which allows a considerably smaller region to be modelled [4]. Simulations were performed in the frequency domain for a range of frequencies. Conductors were modelled as coils and the impedance was obtained using the coil-voltage variables. Changes to the meshing sequence, including changes to the mesh-control elements in the geometry definition, were made to give the finer meshing in the radial direction required to model skin effects over the range of frequencies considered. As shown in Fig. 5, the revised mesh is adequate at the upper end of the frequency range for which it was designed.

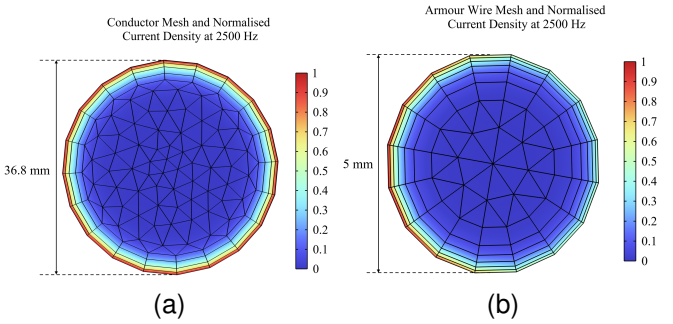

Fig. 5. Conductor and armour mesh plotted against normalised current density norm at 2500 Hz frequency illustrating the skin effect.

A. Modeling Zero-Sequence Currents

Initially, the verification model for the zero-sequence case was a copy of the one for the positive-sequence case. While the imposed currents can easily be changed from positive-sequence to zero-sequence, the field due to zero-sequence currents can extend much further from the cable than field due to a balanced load; hence, the model needs to be extended to much larger distances. However, extending the short-twisted 3D model to include the seabed boundary would not be valid, as the sea does not twist around the cable.

To model these distant fields and include the water and air domains, a 2D finite-element model is appropriate. We therefore incorporate an additional 2D component within the same COMSOL model as the short-twisted 3D component, and couple them together, the 3D component is shown in Fig. 6.

Fig. 7 shows the 2D component, which extends to 2 km from the axis of the cable; as this is sufficient to ensure that the far-field boundaries have negligible effects, simple magnetically insulating boundaries are appropriate here. Half of the geometry is modelled, and a 'Perfect Magnetic Conductor' boundary was used to represent the symmetry plane.

The two components were coupled by a pair of 'Global Equations'. In COMSOL, each 'Global Equation' adds one

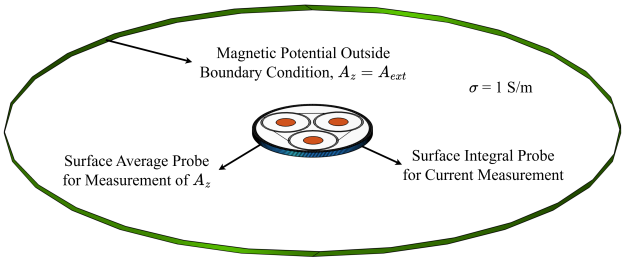

Fig. 6. Boundary conditions and probe definitions of the 3D model implemented in COMSOL Multiphysics.

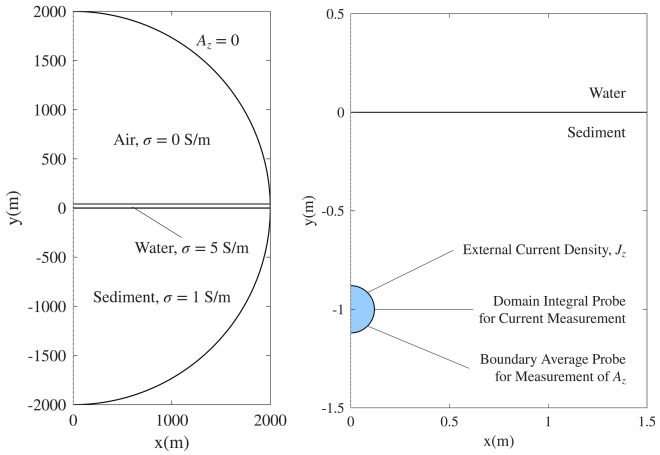

Fig. 7. Boundary conditions, probes and dimensions of the 2D model.

unknown to be found by the solver and has a name that allows this unknown quantity to be used to define source terms within the model and an expression that the solver should try to make equal to zero. We define the expressions that control the global equations using 'Probes', which are derived quantities such as integrals or averages that would usually be calculated in post-processing; defining them as probes makes them available during the solution. The total current in the cable in the 3D component, I_{3D}, was obtained from a surface-integral probe of the tangential component of the H-field at the cable's surface in the 3D model.

In the 2D model, the cable is represented as a coil, and its current, $\frac{1}{2}I_{2D}$ (as the 2D model has only half of the geometry), is set by a global equation that aims to make the average value of the vector-potential component A_z on the surface of the cable in the 2D model equal to the corresponding value in the 3D model; two probes are used to evaluate these averages. In the 3D model, the value of A_z on the far-field boundary is set by a global equation that aims to make $I_{3D} - I_{2D} = 0$; for simplicity, the other components of A are set to zero on this boundary. Notice that only the uniform components of the field at the cable surface are constrained to be equal. As the 3D model represents twisted geometry but the 2D model does not, all the other Fourier components in the 3D model are orthogonal to those in the 2D model.

VI. Verification Results for Positive-Sequence Models

Our validation calculations consider two cable designs. The first is the one described in Case 8 of CIGRE TB 880 [17]; the second uses the same geometry, but with the stainless-steel armour replaced by magnetic armour. For the magnetic armour, we assume that the permeability is 270-80j and the conductivity is taken from Table 1 of IEC 60287 [14] with a temperature of 60°C. The conductivity of lead and copper used are also defined using Table 1 of [14] for the temperatures given in [17].

A. Results for an Export Cable with Stainless Steel Armor

Fig. 8 shows the values of the positive-sequence resistance of this cable obtained from the two models, while Fig. 9 shows the corresponding estimates of the inductance. The absolute percentage is evaluated relative to the FEA solution.

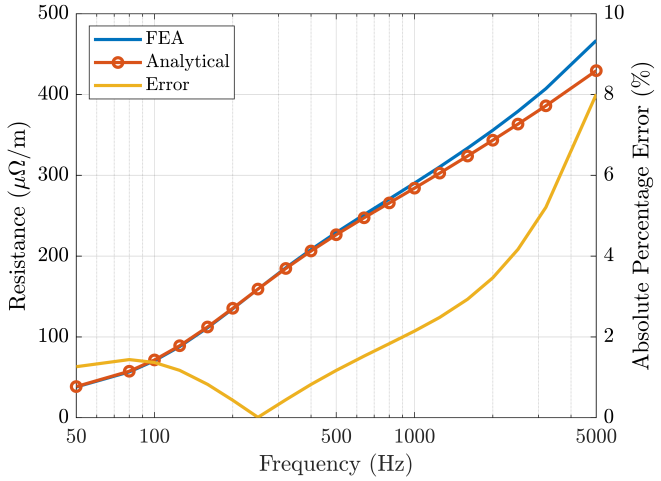

Fig. 8. Analytical calculation and FEA solution of positive-sequence resistance.

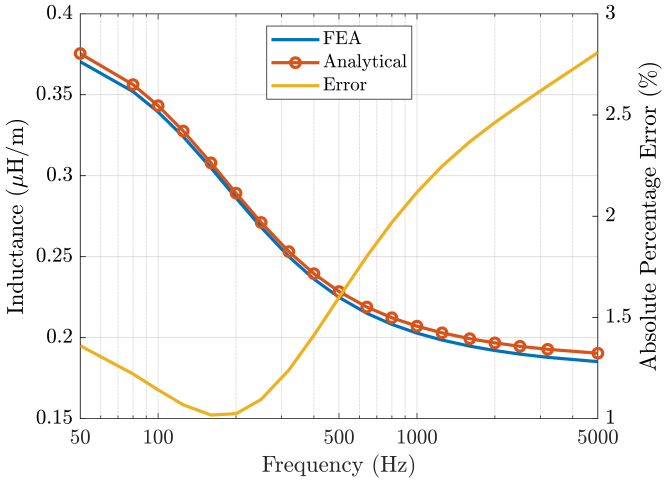

Fig. 9. Analytical calculation and FEA solution of positive-sequence inductance.

For frequencies up to 800 Hz, the resistance and inductance estimates from the two models both agree to within 2%. However, at higher frequencies, the two estimates of resistance begin to diverge; the discrepancy is 4.2% at 2.5 kHz. This is expected; the zero-thickness sheath approximation used by the analytical model suppresses the skin effect in the sheath, which is not negligible at these frequencies; it also overestimates the leakage flux between the conductor and the sheath, but only the contribution from flux flowing within the sheath region is overestimated. As the larger contributions from flux in the insulation and the conductor are not effected, the errors in the inductance calculations are smaller.

B. Results for an Export Cable with Magnetic Steel Armor

The cable considered here has the same geometry, but the stainless-steel armour is replaced by magnetic steel with permeability 270-80j and conductivity taken from Table 1 of IEC 60287 [14] with a temperature of 60°C. Fig. 10 and Fig. 11 show the values of the positive-sequence resistance and inductance of this cable obtained from the two models. These two graphs are very similar to those for the previous case; the graphs of resistance all have 3 significant features in common: at low frequencies, the graphs curve upward, as the sheath currents and losses increase; around 500 Hz, they curve downward, as most of the current now returns in the sheaths, the sheath losses increase more slowly; at high frequencies, the graphs curve upward again, as the skin effect in conductors and sheaths increases.

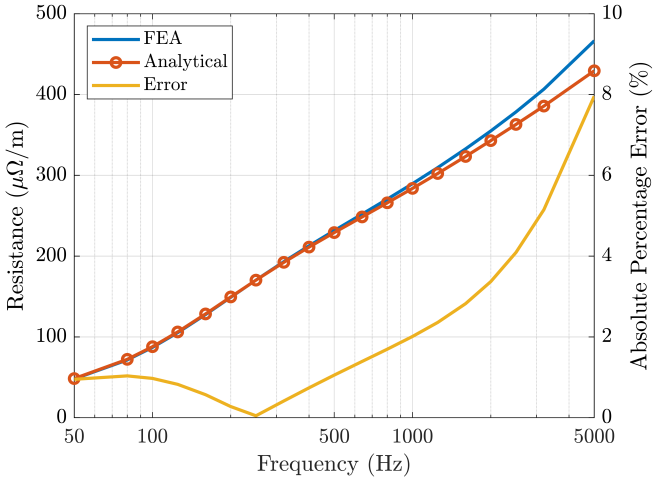

Fig. 10. Analytical calculation and FEA solution of positive-sequence resistance with magnetic armor.

Although the graphs are similar, there are some significant differences; see Fig. 12. At low frequencies, use of magnetic armour increases both the resistance and the reactance.

The reduction in reactance at higher frequencies is counter-intuitive but can be explained. In the single-phase equivalent circuit, the return current flows through the sheath resistance in parallel with the sheath reactance; the reactance of this return path is maximum when the sheath reactance is equal to the sheath resistance. Hence, at higher frequencies, increasing

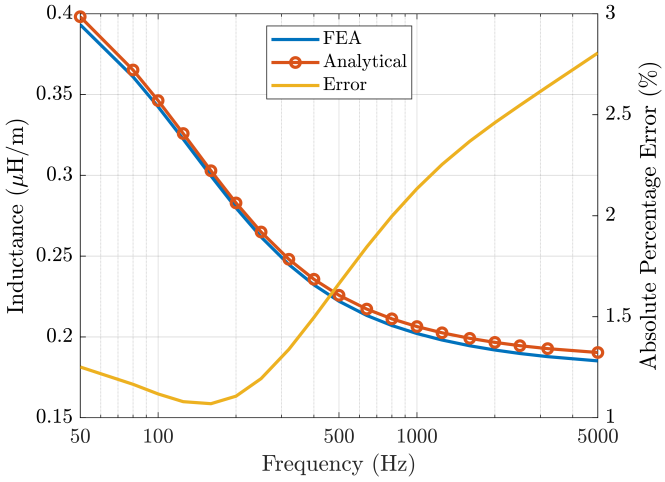

Fig. 11. Analytical calculation and FEA solution of positive-sequence inductance with magnetic armor.

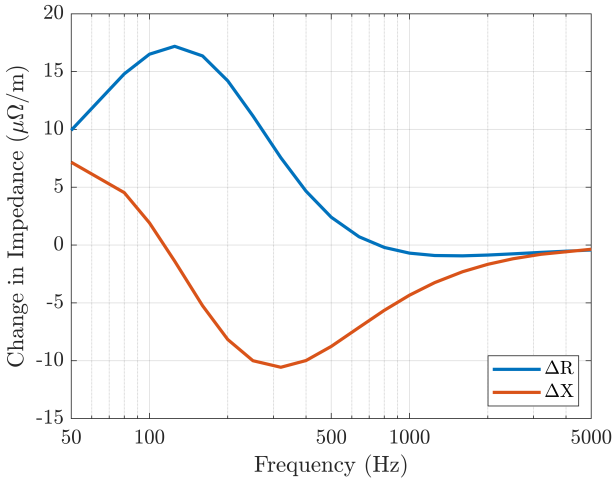

Fig. 12. Effect of magnetic armour on positive-sequence impedance.

the inductance to sheath current reduces the overall reactance. At the highest frequencies, magnetic armour has little effect. This is because most of the current returns in the sheaths, screening the armour from the field of the conductor currents. The maximum increase in the loss is around three times the maximum armor loss; increased sheath currents contribute most to the increase in resistance.

VII. Verification Results for Zero-Sequence Models

For each of the two cables considered above, we compare the values of zero-sequence impedance calculated by the method described in Section III with those from the finite-element models described in Section V.

A. Results for an Export Cable with Stainless Steel Armor

Fig. 13 shows that the two models give very similar estimates of the zero-sequence resistance at frequencies below 2

kHz. However, at higher frequencies, the value given by the finite-element model increases much faster than the value from the analytical model (Fig. 13). As in the positive-sequence case, this is attributed to the skin effect in the sheath, which is not included in the analytical model.

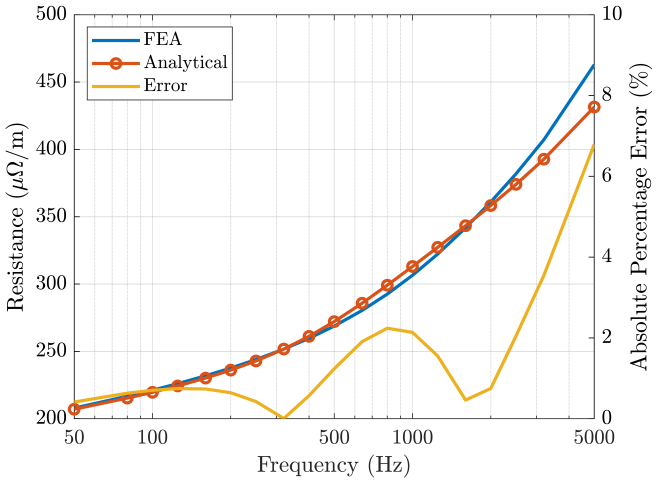

Fig. 13. Analytical calculation and FEA solution of zero-sequence resistance.

Fig. 14 shows the corresponding inductances calculated by the analytical and FEA models. Both methods show significant reduction in inductance as the proportion of the current returning in the sheaths increases.

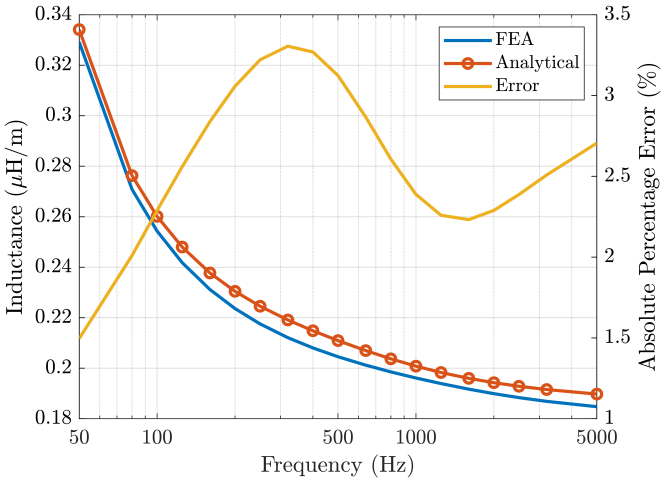

Fig. 14. Analytical calculation and FEA solution of zero-sequence inductance.

The two models give similar values of resistance and reactance. Except for the resistance at frequencies above 3.2 kHz, none of the discrepancies are greater than 3.5%.

B. Results for an Export Cable with Magnetic Steel Armor

The graphs of zero-sequence resistance (Fig. 15) are similar to those for non-magnetic armour, except at low frequencies where both models show lower resistance. This difference is attributed to the lower DC resistance of the magnetic armour

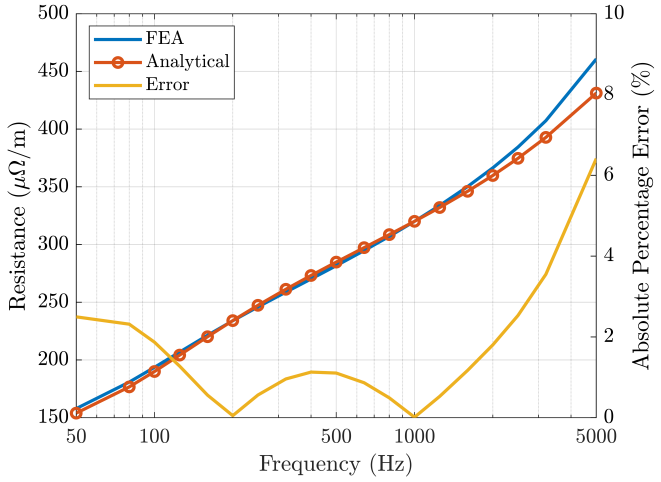

Fig. 15. Analytical calculation and FEA solution of zero-sequence resistance with magnetic armor.

itself (relative to that of stainless steel), which carries a significant proportion of the return current at these frequencies.

The graphs of zero-sequence inductance (Fig. 16) are also similar to those for non-magnetic armour. The two models have slightly larger discrepancies than those for the cable with non-magnetic armour but, except for the resistance at frequencies above 3.2 kHz, none of the discrepancies are greater than 4%.

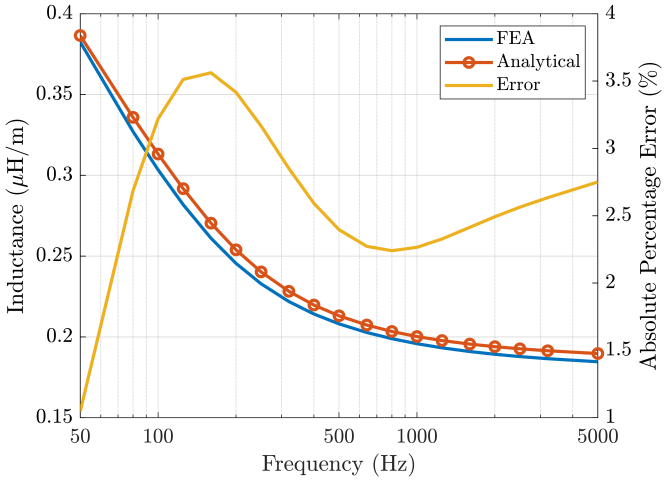

Fig. 16. Analytical calculation and FEA solution of zero-sequence inductance with magnetic armor.

Fig. 17 illustrates the percentage error of the resistance, reactance and total impedance. A positive percentage error indicates that the values calculated analytically are larger than the FEA solution. At higher frequencies, the impedance is dominated by the reactance. Thus, the larger errors in resistance do not contribute significantly to the discrepancies in the overall impedance.

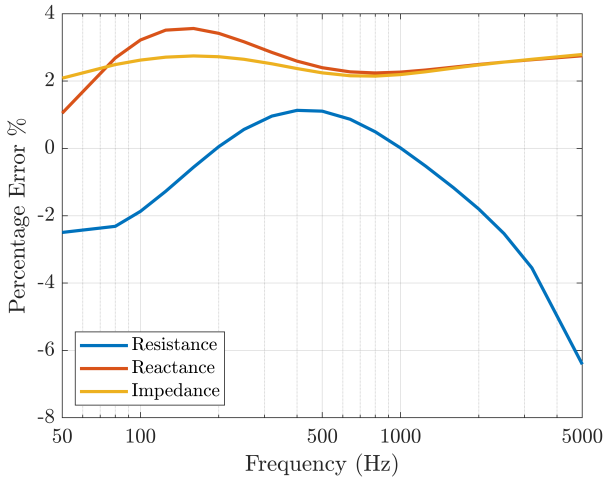

Fig. 17. Comparison of errors in the resistance, reactance and impedance for the zero-sequence solution with magnetic steel armor.

C. Effect of Water Depth

As the analytical model takes the ground-return impedance $R_g + jX_g$ from the infinite-sea model, it ignores the water depth. We have modified the 2D component of the finite-element model to estimate this impedance for various depths of water. While the value of R_g given by the infinite sea model depends only on the frequency, the value from the finite-element model varies significantly with respect to the water depth. Ratios of the values from the finite-element models to those from the infinite-sea model are shown in Fig. 18. Corresponding ratios of reactance values are shown in Fig. 19. An equivalent conductivity of 2.2 S/m was used in the infinite-sea model.

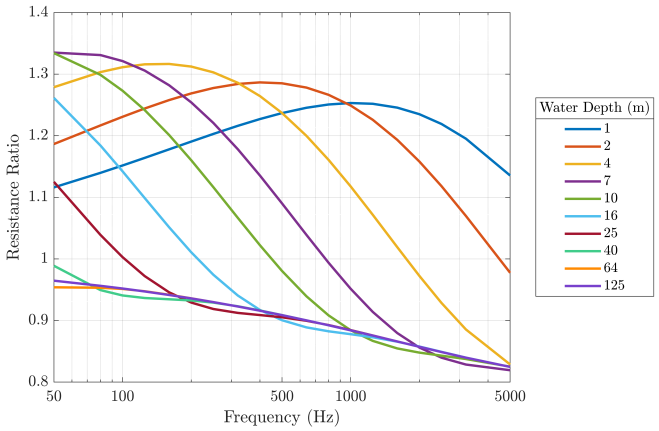

Fig. 18. Effect of water depth on the ground-return resistance. Ratio of the finite element model to infinite-sea model results.

While these discrepancies are substantial, their effects on the zero-sequence impedance of the export cable are less than 1.4%, and for depths above 10 m they are less than 0.6%. The results reported in Sections VII A and VII B above are for a water depth of 40 m.

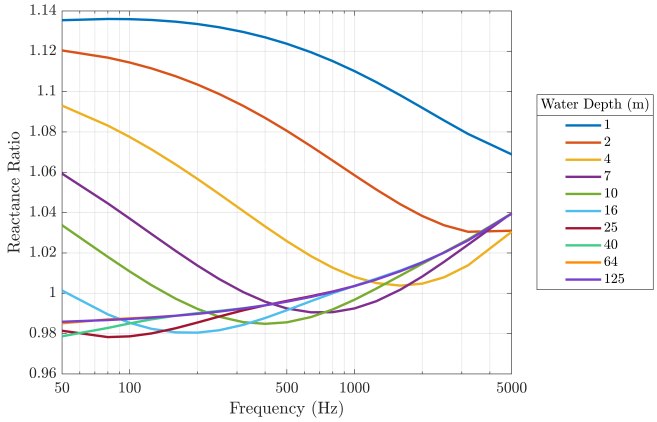

Fig. 19. Effect of water depth on the ground-return reactance. Ratio of the finite element model to infinite-sea model results.

VIII. Conclusion and Future Work

The impedance values obtained from the presented analytical models show good agreement with those from the corresponding finite-element models. For all frequencies between 50 Hz and 5 kHz, the discrepancies in the positive-sequence impedance are all below 2.9% while those for the zero-sequence impedance are all below 3%. These comparisons are all for conventional SL cables with solid sheaths and single-layer armour. Both magnetic and non-magnetic armor was considered.

There seems to be no absolute accuracy requirement for such calculations. In [13], it is suggested that for positive-sequence impedance errors of 2% at power frequency and 15% for harmonics frequencies are acceptable, similar estimates are not provided for zero-sequence impedances. However, greater uncertainties require larger design margins, which may increase costs. We assume that, when the modelling errors are small in relation to the changes in impedance due to likely changes in cable temperatures, there is little value in improving the accuracy. We therefore used our analytical model to estimate the effect of cooling the cable from the hot (maximum continuous rated) values used above to 10°C. We found that, except at frequencies above 1.6 kHz, these effects are larger than the modelling discrepancies.

The proposed method is a more computationally efficient alternative to finite element methods (as it solves under 10 seconds) and more accessible given the provision of Python code with implementation of the method.

We have not attempted to estimate the effects of distributed shunt admittance on the impedances as this would require a different type of model. Our method could be extended to enable the calculation of the full series-impedance matrix required by such model.

The models described in this paper are restricted to cables that have only one screen for each conductor and only single-layer armour. Extending the models to cover these configurations would be useful; in particular, most medium-voltage array cables have wire screens together with water-blocking foil screens. The positive-sequence model does cover the double-armour case if the inner armour is non-magnetic,

but the zero-sequence model would need to be redefined as a complex-impedance-matrix model for either double-screen or double armour cases to be modelled. Extending the positive-sequence model to cover cables with both wire screens and foil screens requires only one additional equation to be added to the matrix, but this requires several extra mutual inductances to be defined. A key difficulty in development of these extensions lies in the construction of FEA verification models. Explicitly modelling these more complex geometries in 3D is probably impractical due to geometric complexity; instead we could model a screen or armour layer as a tube with anisotropic conductivity to represent the heading direction of its wires. Additionally, while solenoidal inductance is included in both our positive-sequence and zero-sequence models, eddy currents driven by the associated axial flux are not considered. The inclusion of these eddy currents might also be considered.

APPENDIX

The model was solved on a 13th Gen Intel® Core™ i7-13700 (2.10 GHz) processor with 64 GB RAM. The COMSOL model solving time was approximately a minute, the solving time of the method implemented in Python was under 10 s.

The cable used for validation of the method presented in this work is shown in Fig. 20. The relevant dimensions and material parameters are presented in Table I, only the resistivity and permeability of the armour vary between the two modelled cables.

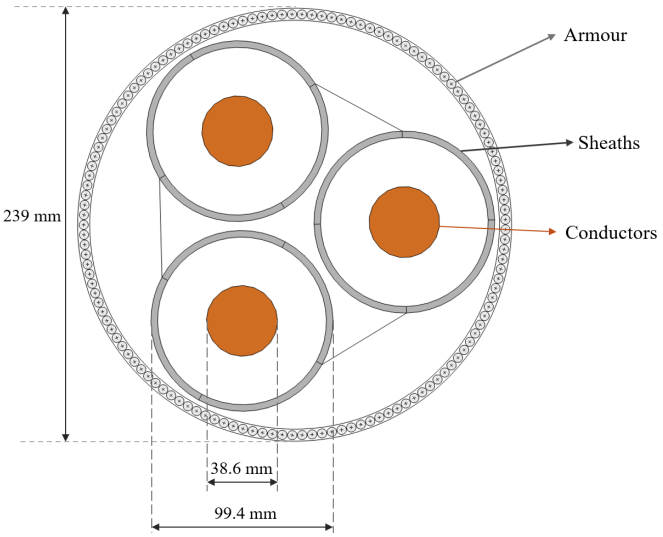

Fig. 20. Cross section of cable used for validation, modelled after Case 8 cable from CIGRE 880 Technical Brochure [17].

ACKNOWLEDGMENTS

The work described in this paper was funded by and developed during the Carbon Trust Offshore Wind Accelerator (OWA) 'Sequence Impedance of Submarine Cables (SISC)' project, and is published with the permission of the OWA.

TABLE I
CABLE PARAMETERS

Electromagnetic	
Voltage	220 [kV]
Current	1000 [A]
Geometric	
Conductor diameter	38.6 [mm]
Diameter over insulation (including semiconducting tapes and insulation)	92.2 [mm]
Lead sheath thickness	3.6 [mm]
Distance between conductor axes	104.6 [mm]
Lay length of power cores	2750 [mm]
Number of armour wires	133
Armour wire diameter	5 [mm]
Central diameter of armour ring	232 [mm]
Lay length of armour	2900 [mm]
Material	
Copper conductor resistivity at 20°C	1.724e-8 [Ωm]
Lead sheath resistivity at 20°C	21.4e-8 [Ωm]
Armour steel wire resistivity at 20°C	70e-8/13.8e-8 [Ωm]
Armour relative permeability	1/270-80i

REFERENCES

[1] CIGRE WG B1.30, "Cable systems electrical characteristics," Technical Brochure 531, pp. 1–143, 2013.
[2] J. Bremnes, G. Evenset, and R. Stølan, "Power loss and inductance of steel armoured multi-core cables: comparison of iec values with 2.5d fea results and measurements," in *Proc. of Cigre Session*, 2010.
[3] COMSOL Multiphysics, "Cable tutorial series part 8: Submarine cable - inductive effects 3d," 2020.
[4] A. I. Chrysochos, D. Chatzipetros, C. K. Traianos, K. Bitsi, J. Morales, H. Xue, and J. Mahseredjian, "Impact of solenoid effects on series impedance of three-core armoured cables," *Electric Power Systems Research*, vol. 220, p. 109296, 2023.
[5] R. Benato and S. D. Sessa, "A new multiconductor cell three-dimension matrix-based analysis applied to a three-core armoured cable," *IEEE Transactions on Power Delivery*, vol. 33, pp. 1636–1646, 2018.
[6] R. Benato, S. D. Sessa, G. Gardan, F. Palone, and F. Sanniti, "Experimental harmonic validation of 3d multiconductor cell analysis: Measurements on the 100 km long sicily-malta 220 kv three-core armoured cable," *IEEE Transactions on Power Delivery*, vol. 37, pp. 573–581, 2022.
[7] R. Benato, S. D. Sessa, and M. Forzan, "Experimental validation of three-dimension multiconductor cell analysis by a 30 km submarine three-core armoured cable," *IEEE Transactions on Power Delivery*, vol. 33, pp. 2910–2919, 2018.
[8] U. R. Patel, B. Gustavsen, and P. Triverio, "Proximity-aware calculation of cable series impedance for systems of solid and hollow conductors," *IEEE Transactions on Power Delivery*, vol. 29, pp. 2101–2109, 2014.
[9] B. Gustavsen, M. Høyer-Hansen, P. Triverio, and U. R. Patel, "Inclusion of wire twisting effects in cable impedance calculations," *IEEE Transactions on Power Delivery*, vol. 31, pp. 2520–2529, 2016.
[10] L. Giussani, L. D. Rienzo, M. Bechis, and C. de Falco, "Fully coupled computation of losses in metallic sheaths and armor of ac submarine cables," *IEEE Transactions on Power Delivery*, vol. 37, no. 5, pp. 3803–3812, 2022.
[11] CIGRE WG B1.64, "Losses in armoured three core power cables," Technical Brochure 908, pp. 1–159, 2023.
[12] K. F. Goddard, J. A. Pilgrim, R. Chippendale, and P. L. Lewin, "Induced losses in three-core SL-type high-voltage cables," *IEEE Transactions on Power Delivery*, vol. 30, pp. 1505–1513, 6 2015.
[13] T. Kvartz, A. C. Garolera, Z. Huang, and O. Thyrvin, "Sequence impedance of submarine cables," in *Cigre Session*, Paris, France, 2022.
[14] "BS IEC 60287-1-1:2023 - Electric cables — Calculation of the current rating," The British Standards Institution, Standard, Jun. 2023.
[15] A. E. Kennelly, F. A. Laws, and P. H. Pierce, "Experimental researches on skin effect in conductors," in *Panama-Pacific Convention of the American Institute of Electrical Engineers*. American Institute of Electrical Engineers, September 1915, pp. 1983–2009.
[16] P. Hammond, *Applied Electromagnetism*. Pergamon Press, 1971, pp. 79–86.
[17] CIGRE WG B1.56, "Power cable rating examples for calculation tool verification," Technical Brochure 880, pp. 1–331, 2022.

IX. Biography Section

Kevin Goddard received a BSc in Electrical Engineering from University of Southampton, England in 1982. He obtained his PhD in 1992 for work on stray fields in the stator frames of electrical machines, also from University of Southampton. After short periods in industry, he became a Research Fellow at University of Southampton. He worked on electromagnetic design and numerical modeling of electrical machines. His recent work involved electromagnetic and thermal modeling in cables. Dr. Goddard is a member of the IET.

Joanna Rzempołuch was born in Warsaw, Poland in 2001. She received her BEng degree in Electrical Engineering from the University of Southampton in 2023. She is currently pursuing a PhD degree in Electrical and Electronics Engineering at the same university. Her main research interests are computational modeling and high voltage submarine cables.

Sunny Chaudhary , born in 1995 in Meerut, India, completed his MSc in Energy and Sustainability in Electrical Power Engineering at the University of Southampton, UK, in 2017. Subsequently, he earned his Ph.D. in Electrical Engineering from the University of Southampton, UK, in 2023. Currently, he is a Research Fellow within the Electric Power Engineering group at the University of Southampton. His research interest include thermal modeling and polymer nanocomposite - based insulation materials.

George Callender was born in Basildon, U.K., in 1991. He received the M.Sci. degree (Hons.) in natural sciences (maths and physics) from the University of Durham, Durham, U.K., in 2013, and the Ph.D. degree in electrical engineering from the University of Southampton, Southampton, U.K., in 2018. He is currently an Associate Professor at the University of Southampton. His research interests include partial discharge phenomena and the thermal modeling of high voltage plant.

Paul Lewin was born in Ilford, Essex, in 1964. He received the B.Sc. (Hons.) and the Ph.D. degrees in electrical engineering from the University of Southampton, Southampton, U.K., in 1986 and 1994, respectively. He joined the academic staff of the University in 1989 and is the Director of the Tony Davies High Voltage Laboratory. His research interests include the generic areas of applied signal processing and control. Within high voltage engineering this includes condition monitoring of HV cables and plant, surface charge measurement, HV insulation/dielectric materials and applied signal processing. Since 1996, he has been received funding and grants in excess of £32M, supervised over 50 graduate students to successful completion of their doctoral theses and authored or coauthored more than 600 refereed conference and journal papers in these research areas. He is a Chartered Engineer, a Fellow of the IET, and former President of the IEEE Dielectrics and Electrical Insulation Society.